Study on the Application of Shear-wave Elastography to Thin-layered Media and Tubular Structure: Finite-element Analysis and Experiment Verification

(Shear-wave Elastography 法の
薄板状と円筒状の媒質への適用に関する研究：
有限要素解析と実験的検証)

張 俊根

Jang Jun-keun

Japanese Journal of Applied Physics **55**, 07KF08 (2016)
http://doi.org/10.7567/JJAP.55.07KF08

REGULAR PAPER

Study on the application of shear-wave elastography to thin-layered media and tubular structure: Finite-element analysis and experiment verification

Jun-keun Jang*, Kengo Kondo, Takeshi Namita, Makoto Yamakawa, and Tsuyoshi Shiina

Department of Human Health Sciences, Graduate School of Medicine, Kyoto University, Kyoto 606-8507, Japan

*E-mail: jangjunkeun@yahoo.co.jp

Received November 15, 2015; revised February 14, 2016; accepted March 23, 2016; published online June 14, 2016

Shear-wave elastography (SWE) enables the noninvasive and quantitative evaluation of the mechanical properties of human soft tissue. Generally, shear-wave velocity (C_S) can be estimated using the time-of-flight (TOF) method. Young's modulus is then calculated directly from the estimated C_S. However, because shear waves in thin-layered media propagate as guided waves, C_S cannot be accurately estimated using the conventional TOF method. Leaky Lamb dispersion analysis (LLDA) has recently been proposed to overcome this problem. In this study, we performed both experimental and finite-element (FE) analyses to evaluate the advantages of LLDA over TOF. In FE analysis, we investigated why the conventional TOF is ineffective for thin-layered media. In phantom experiments, C_S results estimated using the two methods were compared for 1.5 and 2% agar plates and tube phantoms. Furthermore, it was shown that Lamb waves can be applied to tubular structures by extracting lateral waves traveling in the long axis direction of the tube using a two-dimensional window. Also, the effects of the inner radius and stiffness (or shear wavelength) of the tube on the estimation performance of LLDA were experimentally discussed. In phantom experiments, the results indicated good agreement between LLDA (plate phantoms of 2 mm thickness: 5.0 m/s for 1.5% agar and 7.2 m/s for 2% agar; tube phantoms with 2 mm thickness and 2 mm inner radius: 5.1 m/s for 1.5% agar and 7.0 m/s for 2% agar; tube phantoms with 2 mm thickness and 4 mm inner radius: 5.3 m/s for 1.5% agar and 7.3 m/s for 2% agar) and SWE measurements (bulk phantoms: 5.3 m/s ± 0.27 for 1.5% agar and 7.3 m/s ± 0.54 for 2% agar).

1. Introduction

Many techniques have been developed to evaluate the elastic properties of human soft tissue because elastic properties are correlated with pathological changes of soft tissue.[1,2] Ultrasound elastography is a noninvasive, precise technique used to assess the stiffness of biological tissue.[3–7] The two main categories of ultrasound elastography are static elastography and dynamic elastography. In static elastography, a strain map is estimated and superimposed on a B-mode image to distinguish suspicious lesions from normal tissue. This strain map can be obtained by comparing consecutive displacement distributions before and after quasi-static compression induced by manually pressing an ultrasound probe on the interrogated tissue.[8,9] However, this technique cannot provide the quantitative mapping of local stiffness due to an inverse problem, and it depends on the operator's skill level.[10,11] In contrast, dynamic elastography is based on the fact that we can deduce Young's modulus (E) of soft tissue from shear-wave velocity (C_S) using Eq. (1), where ρ denotes density.[12] Therefore, the accurate estimation of shear-wave velocity in dynamic elastography is essential.

$$E = 3\rho C_S^2. \tag{1}$$

Shear waves can be generated using either an external monochromatic vibrator[13] or acoustic radiation force (ARF).[12] Shear-wave elastography (SWE), which is based on ARF, has gained considerable attention because of its quantitativeness, reproducibility, and simplicity of use.[14] This emerging modality has been validated for unbounded homogeneous organs such as the breast and the liver.[15,16] These organs are assumed to be purely elastic infinite media, so the influence of their boundary conditions can be neglected. However, shear waves propagating into thin-layered media (e.g., skin layer, cornea, and arterial wall) suffer from dispersion effects, which means that their propagation speeds differ at each frequency. Recently, leaky Lamb dispersion analysis (LLDA), where shear waves propagating into thin media were modeled as leaky Lamb waves, has been proposed to overcome this problem.[17] However, it is still unclear why the conventional time-of-flight (TOF) method is ineffective for estimating the shear-wave velocity of thin-layered media. Moreover, it must to be clarified whether and why LLDA can also be applied to a tube structure such as an arterial wall, because Lamb waves are originally guided waves propagating in a thin plate.

In this study, we performed experimental and finite-element (FE) analyses to evaluate the effectiveness of LLDA over the conventional TOF method. In FE analysis, we investigated why the conventional TOF method is ineffective for thin-layered media. In phantom experiments, the simulation results were verified for 1.5 and 2% agar thin-layered plates and thin-walled tube phantoms. Furthermore, whether LLDA can be applied to a tubular structure was discussed. We confined our attention to the structural effects of media on C_S estimation results; thus, effects of cyclic fluctuations caused by heartbeat or respiration were not considered in this study.

2. Statement of the problem

Figure 1 illustrates SWE measurements for three phantoms with the same agar concentration: bulk phantom [Fig. 1(a)], thin-layered plate phantom [Fig. 1(b)], and thin-walled tube phantom [Fig. 1(c)]. These results were measured using a modified Aixplorer® ultrasound system (Supersonic Imagine) and an SL15-4 linear array probe. Although all of the homogeneous phantoms were made of the same concentration of 1.5% agar, mean values of Young's modulus (E) and shear-wave velocity (C_S) differed. C_S in Fig. 1 was derived from the Young's modulus measured using the Aixplorer® ultrasound system because this ultrasound system yields E from the estimated C_S. Moreover, the measurements for thin-layered plate and thin-walled tube phantoms indicated a lower degree of evaluation than that for the bulk phantom. This discrepancy in C_S resulted from the structural effects of the interrogated media. Therefore, we reviewed

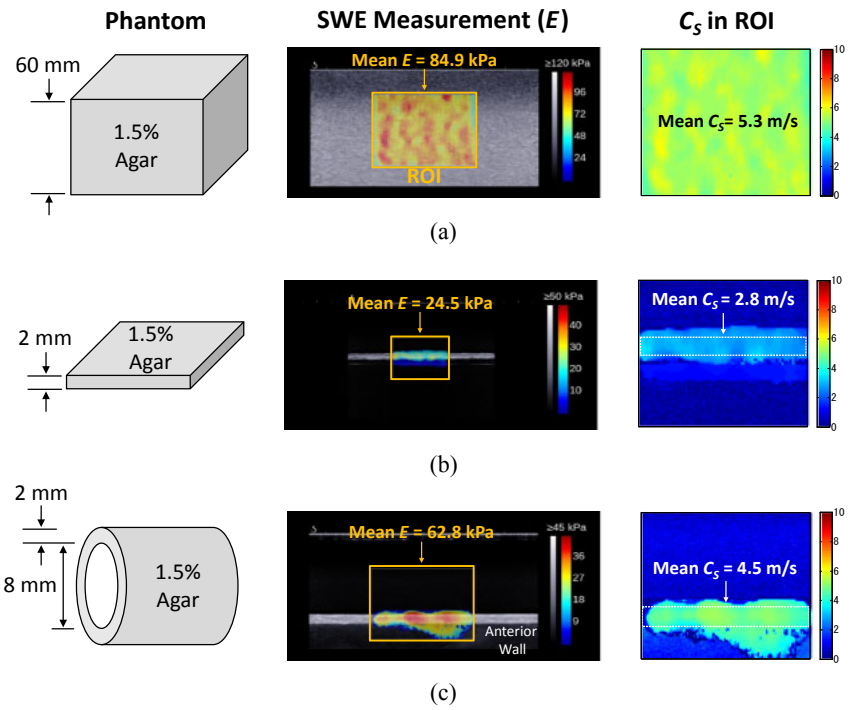

Fig. 1. (Color online) SWE measurements (Young's modulus, E) for 1.5% agar bulk phantom (a), 1.5% agar thin-layered plate (b), and 1.5% agar thin-walled tube phantom (c). The shear-wave velocity (C_S) in the ROI was calculated from $C_S = \sqrt{E/3\rho}$, where ρ is the density.

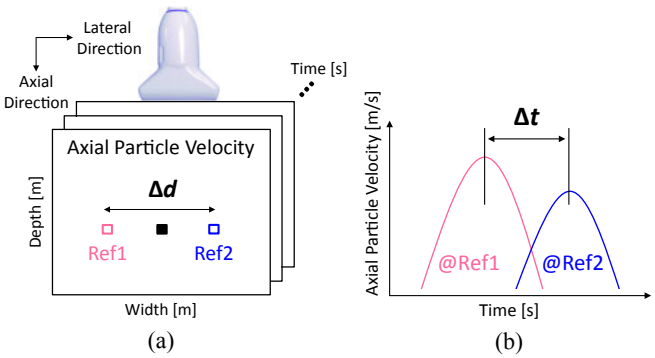

Fig. 2. (Color online) Scheme of the conventional TOF method: reference pixel designation (a) and travel time estimation (b).

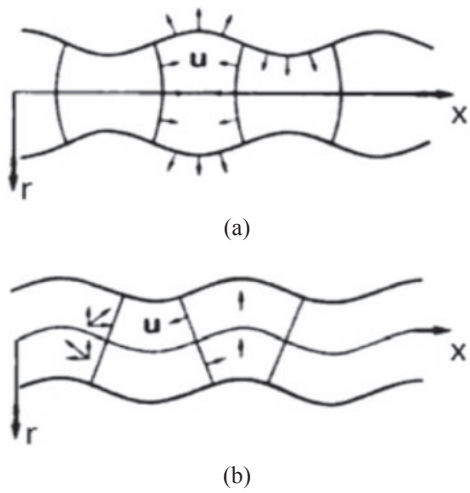

Fig. 3. Symmetric mode (a) and antisymmetric mode (b) of leaky Lamb waves. Here, $\boldsymbol{u}$ denotes the displacement vector in the plate.

conventional C_S estimation and LLDA, compared the C_S results estimated by the two methods, and discussed the effectiveness of LLDA over TOF.

3. Shear wave velocity estimation

3.1 Time-of-flight method

Because shear waves propagate along the lateral direction in the setup depicted in Fig. 2(a), the travel time (Δt) of shear waves and the distance (Δd) between two reference pixels (ref 1 and ref 2) located at the same depth are needed to estimate C_S ($= \Delta d/\Delta t$) at the center black-filled pixel being interrogated. First, we designated the two reference pixels equally spaced from the interrogated pixel [Fig. 2(a)]. Second, the travel time between the two reference pixels was calculated by performing a cross-correlation on axial particle velocity data with respect to time [Fig. 2(b)]. Finally, these procedures were repeated for the entire pixel area of the particle velocity data to estimate the C_S distribution. However, this method can be applied to only unbounded media whose boundary conditions can be neglected.

3.2 LLDA

The frequency of shear waves induced by ARF typically ranges from 1 to 2000 Hz; therefore, shear wavelength becomes 1 to 20 mm in human soft tissue. Shear waves in thin-layered organs (e.g., skin layer, cornea, and arterial wall) whose thickness ($\leq$1 mm) is smaller than shear wavelength, propagate as guided waves, especially Lamb waves. These organs are surrounded by soft tissue whose Young's modulus is typically $\leq$10 kPa or similar to that of a fluid where shear waves cannot propagate; thus, shear waves propagating into thin organs can be modeled by leaky Lamb waves. Furthermore, an axially applied ARF induces mainly antisymmetric modes in thin organs [Fig. 3(b)], and the frequency component of shear waves is mainly located in the low-frequency region. This study thus focused on the first antisymmetric mode (A0) of leaky Lamb waves.[17]

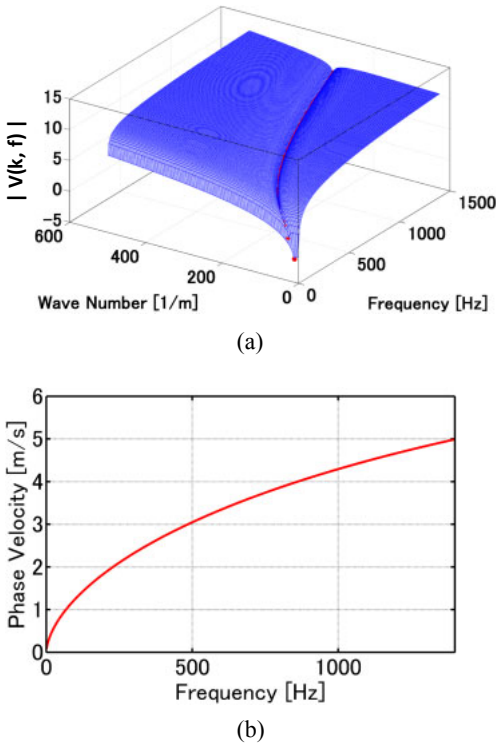

Fig. 4. (Color online) Absolute value of dispersion equation of the first antisymmetric mode of leaky Lamb waves (a) and dispersion curve obtained from a minimization algorithm (b) when $C_L = 1540\,\mathrm{m/s}$, $C_S = 10\,\mathrm{m/s}$, and $h = 1\,\mathrm{mm}$.

The most notable characteristic of guided waves is dispersion effects, which means that their propagation speeds differ at each frequency. First, theoretical dispersion curves of the A0 mode were numerically calculated using Eq. (2), where C_L is the longitudinal velocity of the thin medium, C_S is the shear wave velocity of the thin medium, C_0 is the longitudinal velocity of the surrounding fluid, ρ is the thin medium density, ρ_0 is the surrounding fluid density, h is the thickness of the medium, k is the wave number, and f is the frequency. The dispersion equation, however, contains a complex term; therefore, its absolute value was obtained, and then a minimization algorithm was applied to the absolute value [Fig. 4(a)] to calculate theoretical dispersion curves [Fig. 4(b)].[18] Finally, the theoretical curves were fitted to the experimental curves to estimate shear-wave velocity using the least-mean-squares method. For curve fitting, root-mean-square error (RMSE) was defined by Eq. (3), where V is the theoretical dispersion curve, $\tilde{V}$ is the experimental dispersion curve, and N is the number of data.

$$k_0^2 + k^2 = \left(\frac{2\pi f}{C_0}\right)^2,$$

$$k_L^2 + k^2 = \left(\frac{2\pi f}{C_L}\right)^2,$$

$$k_S^2 + k^2 = \left(\frac{2\pi f}{C_S}\right)^2,$$

$$V(k,f) = (k^2 - k_S^2)^2 \sin\left(\frac{k_L h}{2}\right)\cos\left(\frac{k_S h}{2}\right) + 4k^2 k_L k_S \cos\left(\frac{k_L h}{2}\right)\sin\left(\frac{k_S h}{2}\right) + i\frac{\rho_0 k_L (2\pi f)^4}{\rho k_0 c_S^4}\cos\left(\frac{k_L h}{2}\right)\cos\left(\frac{k_S h}{2}\right) = 0, \quad (2)$$

$$\mathrm{RMSE} = \sqrt{\frac{\sum_{n=1}^{N}[V(n) - \tilde{V}(n)]^2}{N}}. \quad (3)$$

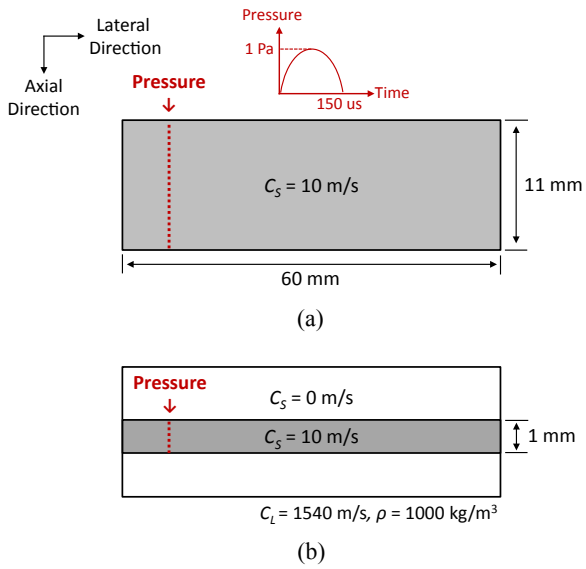

Fig. 5. (Color online) Bulk model (a) and thin-layered plate model (b) of FE analysis.

4. Finite-element analysis

Figure 5 illustrates a bulk model [Fig. 5(a)] and a thin-layered plate model [Fig. 5(b)] of PZFlex® (Weidlinger Associates). PZFlex® is a time-domain FE analysis package for solving acoustic wave propagation and acoustic field problems in 2D and 3D tissue models.[19] Both models were assumed to be linearly elastic, homogeneous materials. Here, C_L was 1540 m/s, ρ was 1000 kg/m^3, the temporal sampling frequency was 10 kHz, and the spatial resolution was 500 µm. To induce shear waves in a thin-layered plate to propagate as leaky Lamb waves, the outer region of the 1 mm plate ($C_S = 10\,\mathrm{m/s}$) was surrounded by a fluid ($C_S = 0\,\mathrm{m/s}$) [Fig. 5(b)]. First, the axially applied pressure (1 Pa amplitude and 150 µs pulse duration) generated shear waves propagating in the lateral direction. Second, axial particle velocity data were obtained by FE analysis without noise. Finally, $\hat{C}_S$ was estimated using the two methods described in the previous section and compared with C_S defined in the FE model (i.e., $C_S = 10\,\mathrm{m/s}$). In addition, we investigated why the general TOF method used in this study cannot accurately estimate the shear-wave velocity of thin-layered media by analyzing shear waves in both models at the time domain.

5. Phantom experiment

5.1 Phantom preparation

Thin-layered plate and thin-walled tube phantoms were prepared to verify the FE analysis results experimentally and to determine whether LLDA, which is based on leaky Lamb waves (i.e., guided waves propagating in a thin plate surrounded with fluid) can also be applied to a tubular

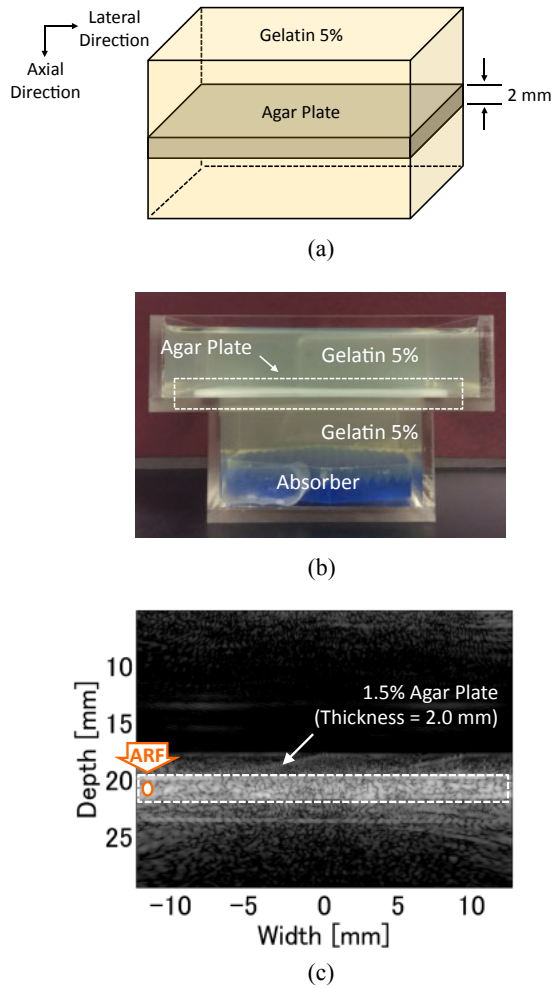

Fig. 6. (Color online) Thin-layered plate phantom: schematic representation (a), phantom photo (b), and B-mode image of a 1.5% agar plate (c).

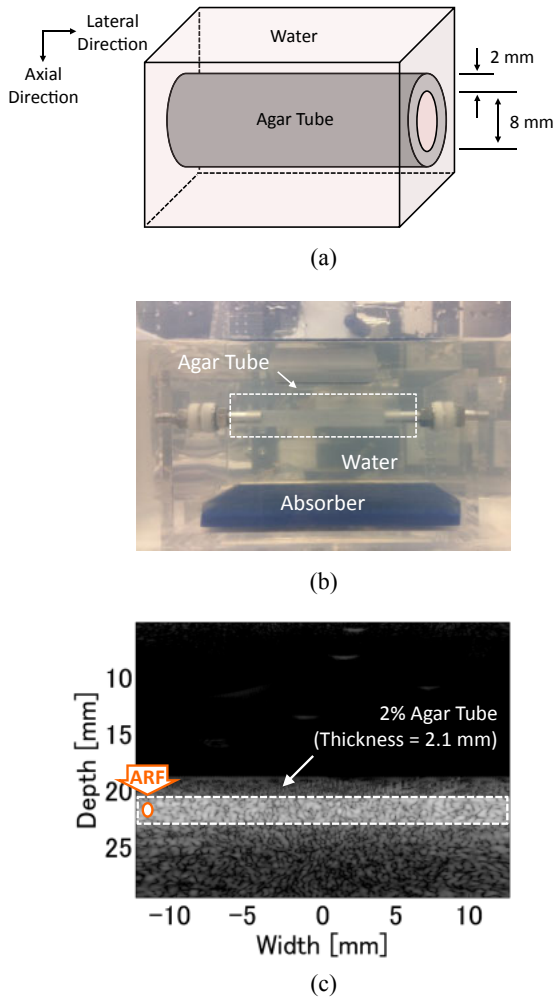

Fig. 7. (Color online) Thin-layered tube phantom: schematic representation (a), phantom photo (b), and B-mode image of the anterior wall of 1.5% agar tube (c).

structure. The phantoms were made of 1.5 and 2% agar with 1% polymer as ultrasonic scatterers. The surrounding material of the plate phantoms was 5% gelatin [Figs. 6(a) and 6(b)], and the tube phantoms were immersed in water [Figs. 7(a) and 7(b)]. The thickness of the plate phantom measured using B-mode images was 2.0 mm [Fig. 6(c)] and that of the tube phantom was 2.1 mm [Fig. 7(c)]. The inner diameter of the tube phantom was 8 mm. Moreover, the effect of the inner radius of the tube was discussed by additionally performing experiments for 1.5 and 2% agar tube phantoms of 2.0 mm thickness and 2.0 mm inner radius. Here, a 1-point ARF, which was applied at the middle point of the agar plate [Fig. 6(c)] and the anterior wall of the agar tube [Fig. 7(c)], was sufficient to generate shear waves propagating along the thin media, because the energy of shear-wave components is confined to the thin media, even though longitudinal components leak into the surroundings.

5.2 Experimental setup and post-processing

In-phase quadrature (IQ) data were obtained using a modified Aixplorer® ultrasound system (Supersonic Imagine) and an SL15-4 linear array probe. The center frequency was 7.5 MHz; the pushing duration of ARF was 150 µs; and the frame rate was 10 kHz. After obtaining IQ data using the Aixplorer® ultrasound system, we computed axial particle velocity by performing 2D autocorrelation on the IQ data.[20] The $\hat{C}_S$ results were then estimated using TOF and LLDA and compared with SWE results measured using the Aixplorer® ultrasound system for agar bulk phantoms. The SWE measurements were 5.3 m/s ± 0.27 for 1.5% agar and 7.3 m/s ± 0.54 for 2% agar.

6. Result and discussion

6.1 FE simulation results

Figure 8 depicts axial particle velocity data of the bulk model [Figs. 8(a) and 8(b)] and plate model [Figs. 8(c) and 8(d)] in the FE analysis, and their lateral profiles extracted from a depth of 5.5 mm at a simulation time of 4.5 ms. In the bulk model, the propagation pattern of shear waves indicated typical bulk waves [Fig. 8(b)]. In contrast, the plate model exhibited complex propagation patterns of guided waves [Fig. 8(d)]. This is because the transverse components of shear waves were reflected at the boundaries and interfered with other shear waves propagating in the plate (C_L = 1540 m/s, C_S = 10 m/s), while the longitudinal components leaked into the surrounding media (C_L = 1540 m/s, C_S = 0 m/s). As a result, the shear waves in the thin plate propagated as guided waves, in particular, leaky Lamb waves. Figure 9 presents the $\hat{C}_S$ results estimated using the general TOF method for the bulk model, and Fig. 10 presents

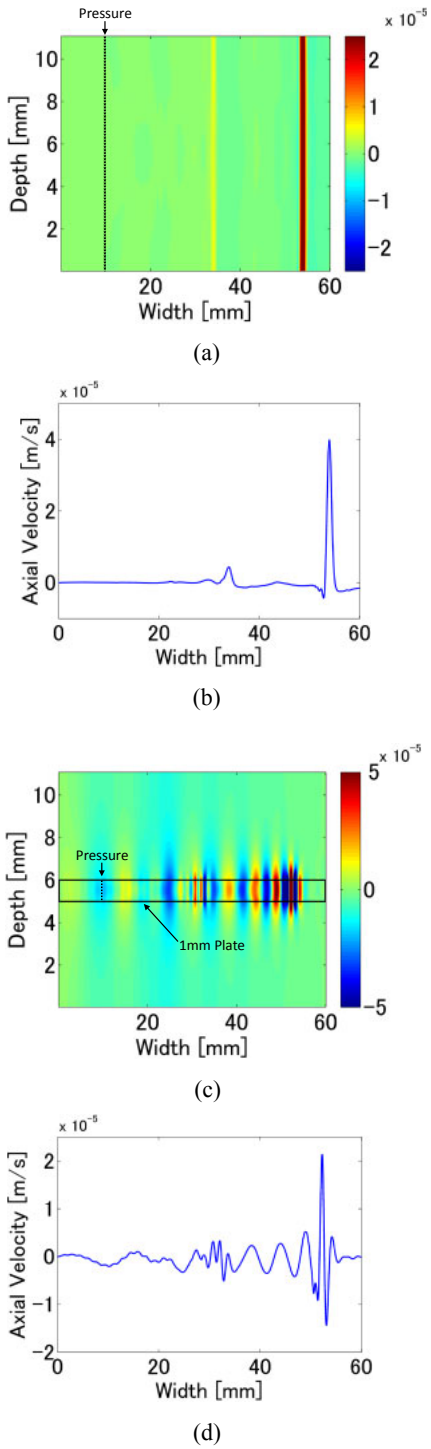

Fig. 8. (Color online) Axial particle velocity data of a bulk model (a) and a thin-plate model (c) at the simulation time of 4.5 m/s. Lateral profiles of the bulk model (b) and the plate model (d) at a depth of 5.5 mm. The waves located between 30 and 40 mm in width were reflected waves at the left-side boundary.

those estimated using TOF and LLDA methods for the plate model. The distance (Δd) of the reference pixels for both Figs. 9 and 10 was set to 4 mm. TOF accurately estimated shear-wave velocity for the bulk model {i.e., mean $\hat{C}_S$ for the entire region of the model agreed with C_S [Fig. 9(a)] and $\hat{C}_S$ at the black-filled pixel $= \Delta d/\Delta t = 4\,\mathrm{mm}/0.4\,\mathrm{ms} = 10\,\mathrm{m/s}$}. For the plate model, however, the mean $\hat{C}_S$ did not agree with C_S [Fig. 10(a)] owing to the complex propagation pattern of shear waves in the plate [Fig. 10(b)]. This

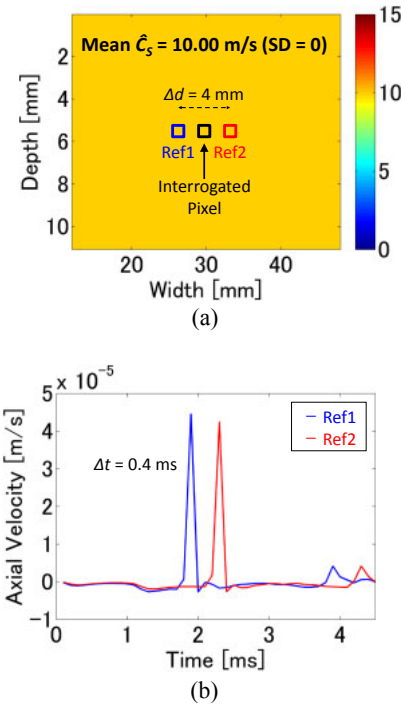

Fig. 9. (Color online) $\hat{C}_S$ distribution estimated by TOF for a bulk model (a). Axial particle velocity data at two reference pixels with respect to time (b). (Mean $\hat{C}_S$ and SD denote the mean value of $\hat{C}_S$ and the standard deviation for the entire region, respectively.)

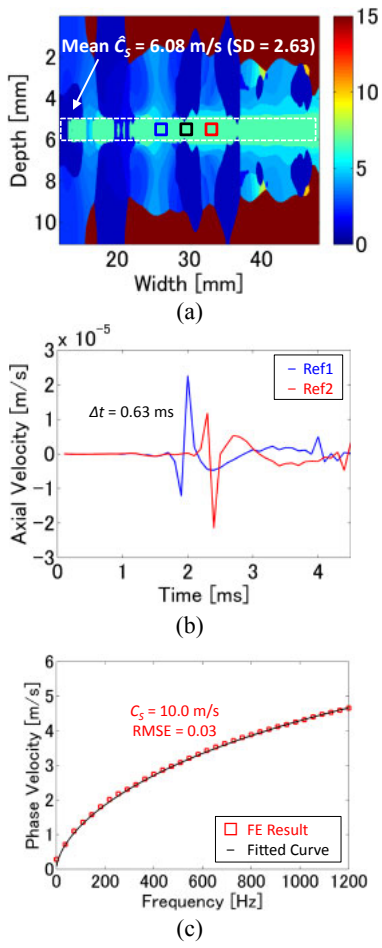

Fig. 10. (Color online) $\hat{C}_S$ distribution estimated by TOF for a plate model (a). Axial particle velocity data at two reference pixels with respect to time (b). Result of LLDA for the plate model. (Mean $\hat{C}_S$ denotes the mean value of $\hat{C}_S$ in the dashed box.)

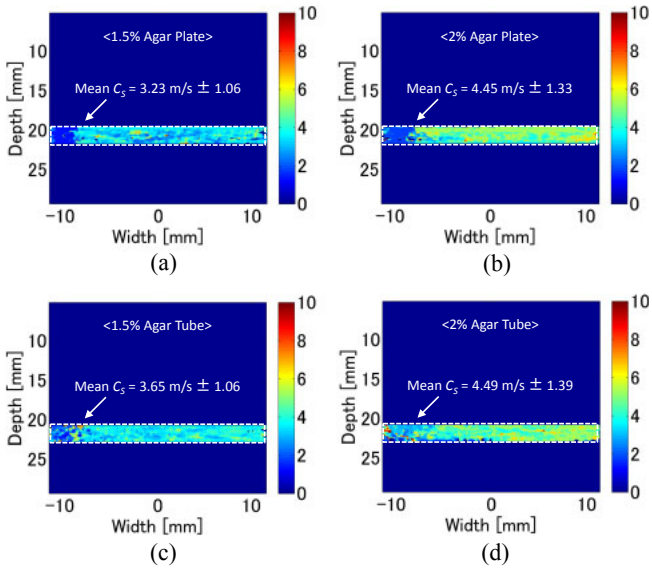

Fig. 11. (Color online) C_S estimation results of TOF for 1.5% plate (a), 2% plate (b), 1.5% tube (c), and 2% tube (d). (Mean C_S denotes the mean value of C_S in the dashed box.)

complexity can lead to an erroneous time lag (Δt), which was estimated using cross-correlation. This erroneous time lag resulted in an incorrect shear-wave velocity estimation (i.e., $\hat{C}_S$ at the black-filled pixel $= \Delta d/\Delta t = 4\,\mathrm{mm}/0.63\,\mathrm{ms} = 6.3\,\mathrm{m/s} \neq C_S$). In contrast, the estimated $\hat{C}_S$ using LLDA coincided perfectly with C_S [Fig. 10(c)].

6.2 Experiment results of TOF

Figure 11 illustrates the shear-wave velocity distributions estimated using TOF for plate and tube phantoms. The distance between reference pixels for all cases was set to 4 mm, which is the same as that in the FE simulation. The mean $\hat{C}_S$ of all phantoms was lower (3.23 m/s ± 1.06 for 1.5% agar plate, 4.45 m/s ± 1.33 for 2% agar plate, 3.65 m/s ± 1.06 for 1.5% agar tube, and 4.49 m/s ± 1.39 for 2% agar tube) than the SWE measurement values (5.3 m/s ± 0.27 for 1.5% agar and 7.3 m/s ± 0.54 for 2% agar). The lower degree of evaluation of the mean $\hat{C}_S$ for plate and tube phantoms than for the bulk phantom is also observed in Fig. 1. This discrepancy can be explained by the erroneous time lag discussed in the previous section.

6.3 Experiment results of LLDA

For LLDA, we extracted one line of axial particle velocity data from the middle depth of the agar plate and the anterior wall of the agar tube [Figs. 12(a) and 13(a)], and performed 2D fast-Fourier transform (FFT) [Figs. 12(b), 13(b), and 13(e)] on the extracted data to obtain experimental dispersion curves. After detecting the energy maxima on the dispersion curves, we calculated phase velocity (C_P) using $C_P = f/k$, where f is the frequency and k is the wave number. Figure 12(c) illustrates the fit results for 1.5 and 2% agar plate phantoms. The $\hat{C}_S$ for 1.5% agar was estimated to be 5.0 m/s (RMSE = 0.13), and that for 2% agar was estimated to be 7.2 m/s (RMSE = 0.12). No significant discrepancies in shear-wave velocity between the LLDA estimation results and the SWE measurements were observed.

Next, we applied LLDA to tubular structures of 4 mm inner radius as shown in Fig. 13. The simulation for a tubular

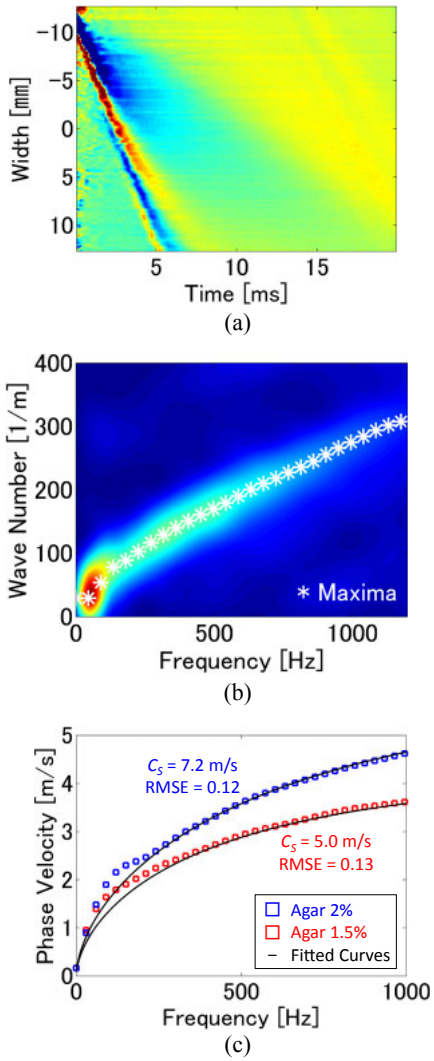

Fig. 12. (Color online) LLDA results for the agar-plate phantoms. Axial particle velocity extracted at the middle depth of the 1.5% agar plate (a). 2D FFT result (b). Curve-fitting results of 1.5 and 2% agar plates (c).

structure needs a 3D FE analysis, and hence, it is difficult because of its computational cost. In that case, experiments using tube phantoms may be effective. Circumferential waves appeared in the extracted particle velocity data [Fig. 13(a)], in contrast to those of the plate phantom [Fig. 12(a)]. Thus, the multiple behaviors of both lateral and circumferential waves were also observed in the 2D FFT result as shown in Fig. 13(b). These multiple behaviors made it difficult to detect the maxima of the main zero-order antisymmetric (A0) Lamb-like mode. Therefore, the circumferential waves were eliminated by applying a 2D window [Fig. 13(c)] that was designed to preserve the content of lateral waves as shown in Fig. 13(d). After this processing, the 2D FFT of windowed velocity data was obtained as shown in Fig. 13(e). Figure 13(f) illustrates the fitting results for 1.5 and 2% agar tube phantoms. Some discrepancies can be seen between the experiment dispersion curves and the fitted ones especially in the low frequency region [Fig. 13(f)]. The discrepancies resulted from the omission of the low frequency in the 2D FFT result [Fig. 13(e)] due to the unavoidable deletion of some lateral waves, and/or from the overlapping of circumferential waves [Figs. 13(a) and 13(d)]. To quantitatively assess this estimation error, the full bandwidth (FBW) of

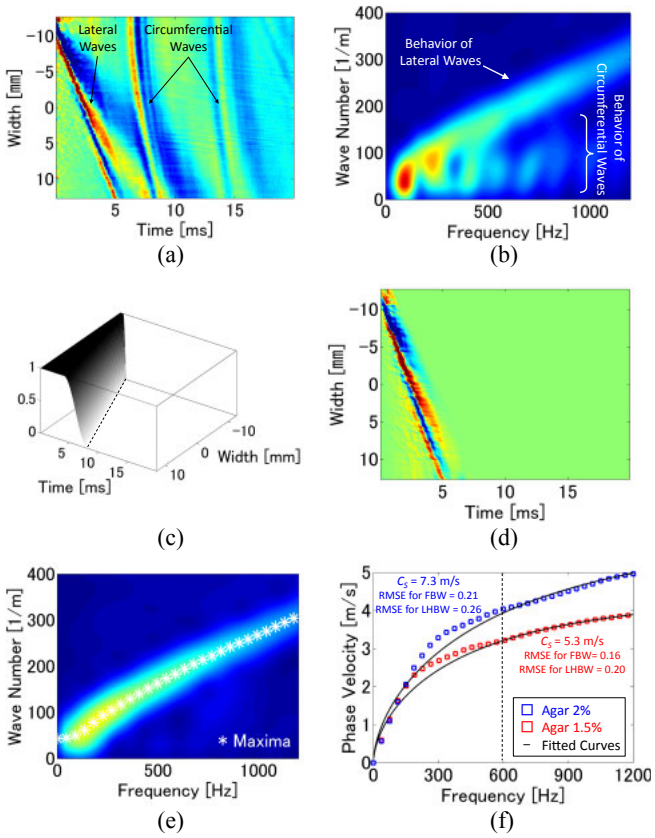

Fig. 13. (Color online) LLDA results for the agar-tube phantoms of 4 mm inner radius. Axial particle velocity extracted at the middle depth of the 1.5% agar tube (a). 2D FFT results of both lateral and circumferential waves (b). 2D window for extracting only lateral waves (c). Extracted lateral waves (d). 2D FFT result of only lateral waves (e). Curve-fitting results of 1.5 and 2% agar tubes (f).

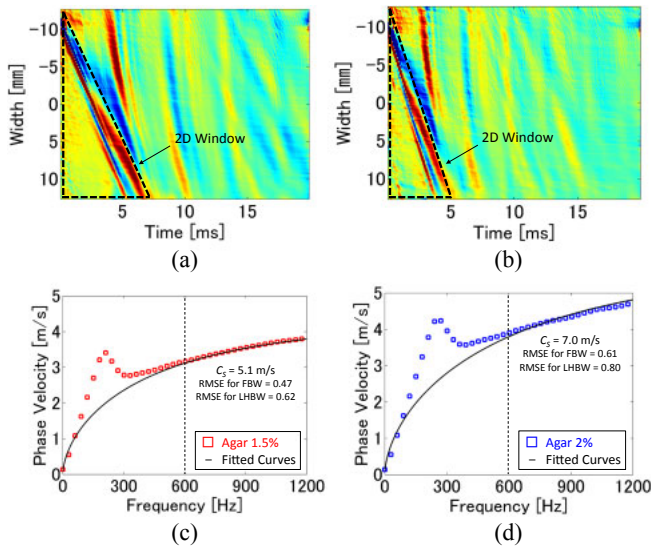

Fig. 14. (Color online) LLDA results for the agar-tube phantoms of 2 mm inner radius. Axial particle velocity and the 2D widow for the 1.5% agar tube (a). Axial particle velocity and the 2D widow for the 2% agar tube (b). Dispersion curve of the 1.5% agar tube (c). Dispersion curve of the 2% agar tube (d).

Table I. Comparison of C_S results estimated by TOF and LLDA for plate and tube phantoms of 2 mm thickness.

Phantom type		SWE measurement for bulk phantom (m/s)	TOF (m/s)	LLDA (m/s)
Agar 1.5%	Plate	5.3 ± 0.27	3.28 ± 1.06	5.0
	Tube[a)]		3.65 ± 1.06	5.3
	Tube[b)]		—	5.1
Agar 2%	Plate	7.3 ± 0.54	4.45 ± 1.33	7.2
	Tube[a)]		4.49 ± 1.39	7.3
	Tube[b)]		—	7.0

a) 4 mm inner radius.
b) 2 mm inner radius.

LLDA was divided into two sections: the lower half-bandwidth (LHBW) and the upper half-bandwidth (UHBW). In the case of tubes, FBW ranged from 0 to 1200 Hz and LHBW from 0 to 600 Hz. As shown in Fig. 13(f), the discrepancies between the experiment dispersion curves and the fitted ones were mainly located in the region of LHBW, so the curve fit was performed only for UHBW and the RMSE for LHBW represented the estimation error caused by the deletion of lateral waves and/or the overlapping of circumferential waves. The $\hat{C}_S$ for 1.5% agar was 5.3 m/s (RMSE for FBW = 0.16, RMSE for LHBW = 0.20), and that for 2% agar was 7.3 m/s (RMSE for FBW = 0.21, RMSE for LHBW = 0.26). Although RMSE for FBW was larger than that of plate phantoms, the LLDA results for tube phantoms also agreed well with the SWE measurements.

The effect of inner radius was also discussed for 1.5 and 2% agar tube phantoms of 2 mm inner radius as shown in Fig. 14. Figures 14(a) and 14(b) represent the axial velocity data, where triangles with a dashed line were the extracted lateral waves, for 1.5 and 2% agar tube phantoms, respectively. Figures 14(c) and 14(d) illustrate the results of curve fitting. The $\hat{C}_S$ for 1.5% agar was 5.1 m/s (RMSE for FBW = 0.47, RMSE for LHBW = 0.62), and that for 2% agar was 7.0 m/s (RMSE for FBW = 0.61, RMSE for LHBW = 0.80). No significant discrepancies between the LLDA estimation results and the SWE measurements were observed even though RMSE for FBW was larger than that of the tube of 4 mm inner radius. The experimental results of the estimated $\hat{C}_S$ using TOF and LLDA are summarized in Table I.

As can be expected, the circumferential waves in Fig. 14(a) appeared earlier in the time domain than those in Fig. 13(a) since the radius decreased. Therefore, this earlier appearance of circumferential waves made it difficult to separate the lateral waves from the circumferential waves. The effect of radius became apparent in the dispersion curves [Figs. 14(c) and 14(d)] where the discrepancies in the lower frequency region indicated a higher degree of evaluation than those of tubes of 4 mm inner radius. Moreover, the RMSE for LHBW increased as the tubes became stiffer for both the cases of Figs. 13 and 14. This implies that the approximation based on the LLDA model degrades when the curvature radius is smaller than the shear wavelength ($\because \lambda_S = C_S/f$). This tends to occur at low frequencies because the curvature radius can be smaller than the shear wavelength at low frequencies. In fact, it was also reported that the dispersion curves of tubes will differ from those of plates especially in the low frequency region as the tube radius decreases.[21)] As a

result, these findings suggest that a higher frequency interval for curve fitting will be needed as the tube becomes smaller in inner radius and/or stiffer. In other words, shear waves of higher frequencies will be needed to accurately estimate shear-wave velocity when the tube radius becomes much smaller than the shear wavelength and/or the tube becomes stiffer.

Another limitation of the application of LLDA to tubular structures should be considered. We proposed a 2D window to extract lateral waves that are necessary for estimating shear-wave velocity in the long axis direction of the tube. However, the slope of the window with respect to the time domain needed to be altered dynamically for different inner radii and stiffnesses. This automatic construction of the 2D window currently cannot be achieved, so this problem should be studied further.

Future studies should focus on the effects of various geometric parameters (e.g., inner radius and thickness) and heartbeat on shear-wave velocity estimation for thin-layered and thin-tubular media using LLDA, as well as on automatic alteration of a 2D window. Furthermore, it is also challenging to estimate C_S or E in the cross-sectional direction of a tube using circumferential waves.

7. Conclusions

In this study, we evaluated the conventional TOF and LLDA methods for estimating the shear-wave velocity of thin-layered media by FE analysis and agar phantom experiments with various structures (plate or tube) and stiffnesses of phantoms. The LLDA method was confirmed to be effective for estimating the shear-wave velocity of a thin medium. In contrast, the conventional TOF method is ineffective for thin media owing to erroneous time estimation for complex guided waves. Furthermore, we showed that LLDA can be applied to tubular structures by eliminating circumferential waves using a 2D window. The effects of the inner radius and stiffness (or shear wavelength) of a tube on the LLDA performance were also discussed experimentally. Future studies should focus on the effects of various geometric parameters and heartbeat. The estimation of shear-wave velocity in the cross-sectional direction of tubular structures is also a challenging topic.

Acknowledgments

This work is partly supported by the Last 5X Innovation R&D Center for a Smart, Happy, and Resilient Society, the COI STREAM Program of Ministry of Education, Culture, Sports, Science and Technology, Japan. We gratefully thank Professor Mami Matsukawa and Mr. Keizirou Murakami of Doshisha University for offering valuable discussions and tube phantoms as a reference.

1) T. A. Krouskop, T. M. Wheeler, F. Kallel, B. S. Garra, and T. Hall, Ultrason. Imaging **20**, 260 (1998).
2) J. Ophir, S. K. Alam, B. Garra, F. Kallel, E. Konofagou, T. Krouskop, and T. Varghese, Proc. Inst. Mech. Eng. Part H: J. Eng. Med. **213**, 203 (1999).
3) Y. Hong, X. Liu, Z. Li, X. Zhang, M. Chen, and Z. Luo, J. Ultrasound Med. **28**, 861 (2009).
4) H. Zhi, B. Ou, B. M. Luo, X. Feng, Y. L. Wen, and H. Y. Yang, J. Ultrasound Med. **26**, 807 (2007).
5) Q. L. Zhu, Y. X. Jiang, J. B. Liu, H. Liu, Q. Sun, Q. Dai, and X. Chen, Ultrasound Med. Biol. **34**, 1232 (2008).
6) K. König, U. Scheipers, A. Pesavento, A. Lorenz, H. Ermert, and T. Senge, J. Urol. **174**, 115 (2005).
7) C. L. de Korte and A. F. W. van der Steen, Ultrasonics **40**, 859 (2002).
8) J. Ophir, B. Garra, F. Kallel, E. Konofagou, T. Krouskop, R. Righetti, and T. Varghese, Ultrasound Med. Biol. **26**, S23 (2000).
9) J. L. Gennisson, T. Deffieux, M. Fink, and M. Tanter, Diagn. Interventional Radiol. **94**, 487 (2013).
10) T. Varghese, Ultrasound Clin. **4**, 323 (2009).
11) J. M. Chang, W. K. Moon, N. Cho, and S. J. Kim, Radiology **259**, 59 (2011).
12) J. Bercoff, M. Tanter, and M. Fink, IEEE Trans. Ultrason. Ferroelectr. Freq. Control **51**, 396 (2004).
13) L. Sandrin, M. Tanter, J. L. Gennisson, S. Catheline, and M. Fink, IEEE Trans. Ultrason. Ferroelectr. Freq. Control **49**, 436 (2002).
14) A. Giannoula, Recent Pat. Electr. Electron. Eng. **3**, 91 (2010).
15) M. Tanter, J. Bercoff, A. Athanasiou, T. Deffieux, J. L. Gennisson, G. Montaldo, M. Muller, A. Tardivon, and M. Fink, Ultrasound Med. Biol. **34**, 1373 (2008).
16) M. Muller, J. L. Gennisson, T. Deffieux, M. Tanter, and M. Fink, Ultrasound Med. Biol. **35**, 219 (2009).
17) M. Couade, M. Pernot, C. Prada, E. Messas, J. Emmerich, P. Bruneval, A. Criton, M. Fink, and M. Tanter, Ultrasound Med. Biol. **36**, 1662 (2010).
18) T. Nguyen, M. Couade, J. Bercoff, and M. Tanter, IEEE Trans. Ultrason. Ferroelectr. Freq. Control **58**, 2305 (2011).
19) M. Tabaru, T. Azuma, and K. Hashiba, Jpn. J. Appl. Phys. **49**, 07HF09 (2010).
20) T. Loupas, J. T. Powers, and R. W. Gill, IEEE Trans. Ultrason. Ferroelectr. Freq. Control **42**, 672 (1995).
21) J. Li and J. L. Rose, Ultrasonics **44**, 35 (2006).

